Supplementary Information (SI) for Energy & Environmental Science.

Supplementary Information for 'Reconstructing the Electrochemistry of Lithium-Ion Batteries Through *Operando* Diffuse Reflectance Spectroscopy'

Arvind Pujari[1,2,3,*], Gratsiela Kostova[2], Hwee Jien Tan[2], Atsunori Ikezawa[3], Hajime Arai[3], and Michael De Volder[2,*]

[1] Cavendish Laboratory, Department of Physics, University of Cambridge, CB3 0HE, UK

[2] Institute for Manufacturing, Department of Engineering, University of Cambridge, CB3 0FS, UK

[3] School of Materials and Chemical Technology, Institute of Science Tokyo, 226-8502, Japan

[*] Address correspondence to ap2180@cam.ac.uk or mfld2@cam.ac.uk

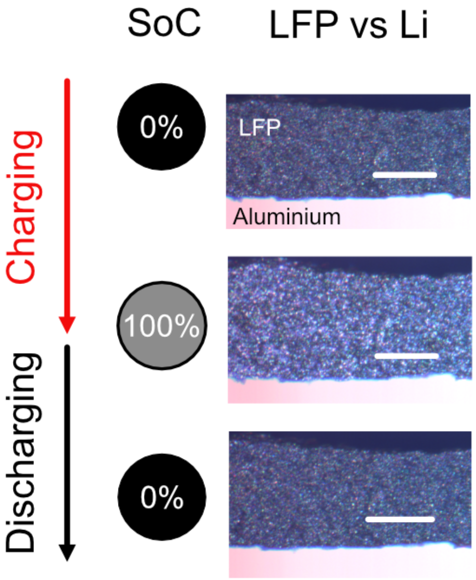

Fig. S1 Cross-sectional images of a $LiFePO_4$ cathode cycled against a Li metal anode obtained through operando confocal microscopy. The cathode gets brighter when charged and darker when discharged, suggesting a correlation between brightness and state-of-charge. All scale bars are 50 µm.

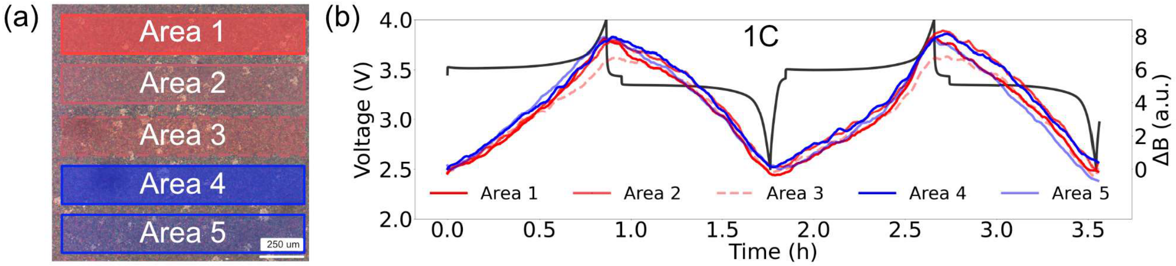

Fig. S2 (a) Operando confocal microscopy images of the electrode surface of a $LiFePO_4$ vs. Li optical coin cell during a 1.25C discharge under a 20× objective. (b) Brightness analysis of five different regions of the electrode. The change in brightness (or reflectance) of the cathode was found to be non-uniform, with the reflectance of Areas 2 and 4 increasing faster than Areas 1 and 2.

Supplementary Note 1: Limitations of Optical Microscopy Techniques for Probing Battery Mechanisms

In confocal microscopy, the image acquisition time is between 60-200 s, which is too slow for accurate operando high-rate charging experiments. A large amount of image-based data is produced during microscopy, especially during extended cycling, and analysis of the data derived is often cumbersome and computationally intensive. Finally, most microscopy based imaging techniques use a single-wavelength imaging source[1–3] due to challenges associated with chromatic aberrations from the glass window of the cell. This prevents a spectroscopic analysis of the cathode, as the reflected (or scattered light) is also of a single wavelength.

The brightness change obtained through optical microscopy of different areas can often be different (as shown in **Fig.** **S2**) due to small variations across the electrode. Although this approach has merits in determining reaction heterogeneity across the electrode surface, it cannot be used as a measure of the state-of-charge of the battery unless the brightness change of several regions is mapped and averaged. This implies that a bulk technique which can acquire an average reflectance measurement across the whole electrode could provide a more representative state of charge measurement of the battery.

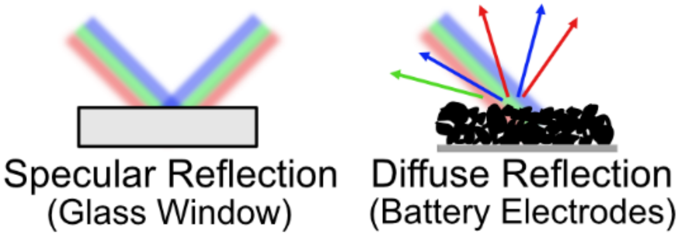

Fig. S3 The two types of reflections possible from optical batteries: specular, from the glass window, and diffuse, from the battery particles.

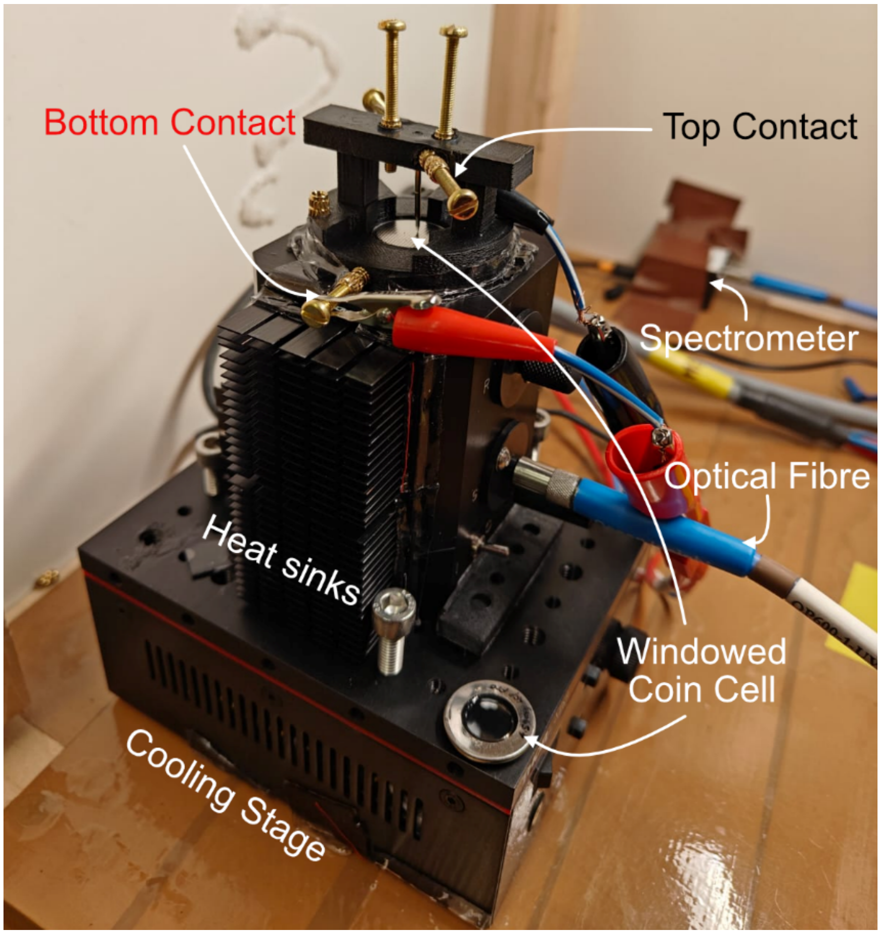

Fig. S4 A digital image of the setup used to perform DRS on batteries. An integrating sphere with an integrated light source is used for all measurements and is connected to a CCD spectrometer by a fibre optic cable. Custom built 3D printed parts are used to create an enclosure for mounting optical coin cells (bottom right) on the entry aperture of the integrating sphere.

Table S1 Pricing and footprint of instruments used for operando electrochemical studies (XRD, NMR, optical microscopy) installed in the UK. The authors acknowledge that the prices can vary considerably based on the exact supplier/configuration and the values shown here are merely indicative.

Type	**Source**	**Price**	**App. Volume ($\mathbf{m^3}$)**
NMR	`https://www.find-tender.service.gov.uk/Notice/016368-2023`	£886,070	2.5
XRD	`https://www.find-tender.service.gov.uk/Notice/040854-2024`	£264,014	5
XRD	`https://www.find-tender.service.gov.uk/Notice/037375-2024`	£300,000	5.5
Optical Microscopy	`https://www.edmundoptics.co.uk/p/motorized-upright-microscope-nikon/52962/`	£27,419	0.25
DRS setup (this paper)	`https://www.oceanoptics.com/accessories/sampling-accessories/integrating-spheres/reflectance-integrating-spheres/`	£5,000	0.001

Supplementary Note 2: Optical Fibre Approaches to Track Battery Reflectance

Several publications have attempted to track the reflection of cathodes previously, mainly using optical fibres. Usually, thin film cathodes are used, however they are unrepresentative of commercial lithium-ion batteries.[4] When optical fibres were used to track the reflectance of composite electrodes, poor signal-to-noise ratios were obtained[5,6] as the fibres are unable to collect a large portion of diffusively reflected light. Optical fibre core diameters typically range from 25 µm - 100 µm, which is much smaller than the size of the electrode, making them unrepresentative of the entire electrode. The small beam size can also lead to local heating effects. Additionally, these experiments are usually performed in non-conventional cell formats, limiting the C-rates that can be used and the relevance for standard battery configurations. Some of these experiments are also performed by inserting an optical fibre into a pouch cell, which can cause changes in the local environment of the battery.[7]

Optical fibres typically track specular reflectance. This is because the illumination and detection pathways are the same. Thus, if the incident light is at 90° to the sample, only reflected light at 90° (i.e. specular reflection) will be captured. An alternative is to illuminate the sample at 45°. This ensures that specular reflection is not captured, but only a small fraction of diffuse reflectance (i.e. the scattered light at 45° is captured).

Supplementary Note 3: Diffuse Reflectance Spectroscopy Setup

An integrating sphere is an optical component consisting of a hollow spherical cavity coated with a white diffusive coating (Spectralon™, reflectance >99% between 400 and 1500 nm) with small entry and exit ports. The light source (output wavelength between 400-2500 nm) is placed at an 8° angle to the normal of the surface of the glass window. Some of the incident light undergoes specular reflection from the glass window and electrolyte and is absorbed by the gloss trap (a black, absorbing surface) located on the other side of the sphere and does not undergo further reflection, preventing the specular component from reaching the spectrometer (See **Fig. 1**(b) of main text). A substantial portion of the incident light is absorbed by the cathode and carbon additive (Super P, which has excellent broadband absorption[8]). The remainder of the light undergoes diffuse reflection from the electrode surface (as powders scatter diffusively) and undergoes Lambertian reflection many times from the surface of the sphere until it reaches the exit port, which is connected to an optical fibre leading to the CCD spectrometer. This allows for a quantification of the diffuse reflected light (intensity at different wavelengths), allowing for the analysis of any new electronic transitions in the material. Due to the tendency of both cathode materials and carbon black to absorb a large proportion of incident light, the amount of light that undergoes diffuse reflection is small. This means that the changes in reflectance are subtle (usually 1-3% when measured against a PTFE reference) and requires a high throughput sensing device such as an integrating sphere that can collect all the diffuse reflectance from the electrode.

As most battery materials are black powders, they have a relatively low optical penetration depth. For example, the optical absorption coefficient of LMO at 620 nm is approximately 9×10^4 cm^{-1}, corresponding to an absorption depth of ∼110 nm[9] (which is the value at which the absorbance falls to 1/e of its original value). Thus, DRS is primarily a sub-surface sensitive technique, especially for transition metal cathodes (assuming average battery particle sizes of 2-10 µm). However, we also study TiO_2, an anode material with a high optical penetration depth (several microns) in the visible regime[10] and highlight the rich variety of information that can be obtained from systems with high optical contrasts.

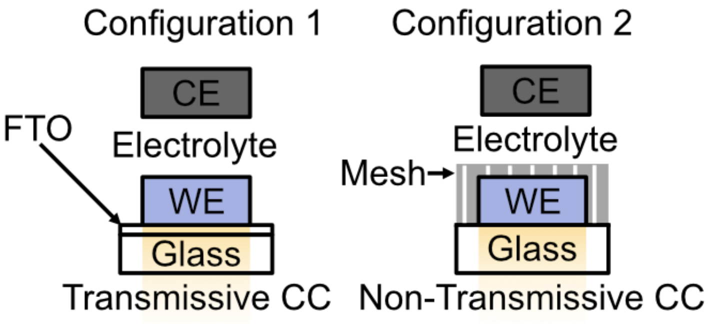

Fig. S5 Optically accessible coin cell configurations used in this study, with either a transparent conductive oxide based current collector in transmissive mode (Configuration 1) or a mesh current collector in non-transmissive mode (Configuration 2).

Supplementary Note 4: Optical Coin Cell Configurations

Here, we use coin cells with an optical window, enabling us to track the reflectance of the entire bottom surface of the electrode. Coin cells are easy to make and have representative stack pressures and electrochemical performance, ensuring that conclusions are drawn from realistic systems. To enable optical access, we use free standing electrodes (shown in **Fig.** S6), made by casting a slurry on glass and then peeling it off after drying, as described in our previous paper.[11]

We utilize the two types of optical coin cell designs demonstrated previously,[11] as shown in **Fig.** S5. The first configuration (transmissive current collector) uses glass coated with fluorine-doped tin oxide (FTO) as the current collector, in a design similar to regular coin cells. However, FTO is several orders of magnitude less conductive than Al or Cu, and has a transmittance of around 80%, resulting in weaker light-battery interactions. The second configuration (non-transmissive current collector) utilizes a metal mesh in an inverted configuration, where the mesh is placed between the separator and electrode, in order to not block light. While this reduces current collector impedance and allows for the use of a glass window (transmittance >95%), this configuration allows for the use of a glass window (transmittance >95%), resulting in more reflected signal.

The light source used in DRS has a wavelength range of 480-2500 nm and an intensity ~50 mW/cm^2. We do not expect white light of this intensity and wavelength range to cause any degradation of the standard LP57 electrolyte used in this study.[12]

In some cases, it may be preferable to perform DRS on commercially relevant electrodes (on metal foil), for instance, for aging studies. In such a case perforated foil can be used as a current collector, as outlined in our previous publication.[13] This enables optical access to the cell while also being compatible with commercial slurry casting processes. The gloss trap in DRS can effectively eliminate specular reflection of the metal foil and allow the measurement of reflectance changes in the active material. A second approach involves laser perforating the electrodes to introduce porosity and placing the active material against the glass window.[13] While this is compatible with traditional electrode foils, only low-rate performance is possible due to the high ionic resistance in the inverted electrode. Alternatively, some publications[14] have reported using single-edged razor blades to pry the electrode off the metal foil, enabling the formation of a free-standing electrode.

Fig. S6 The freestanding electrode obtained after peeling of the battery slurry from a glass plate using a single edged razor blade. 13 mm electrode discs were subsequently punched out of this film. Scale bar is 6 mm.

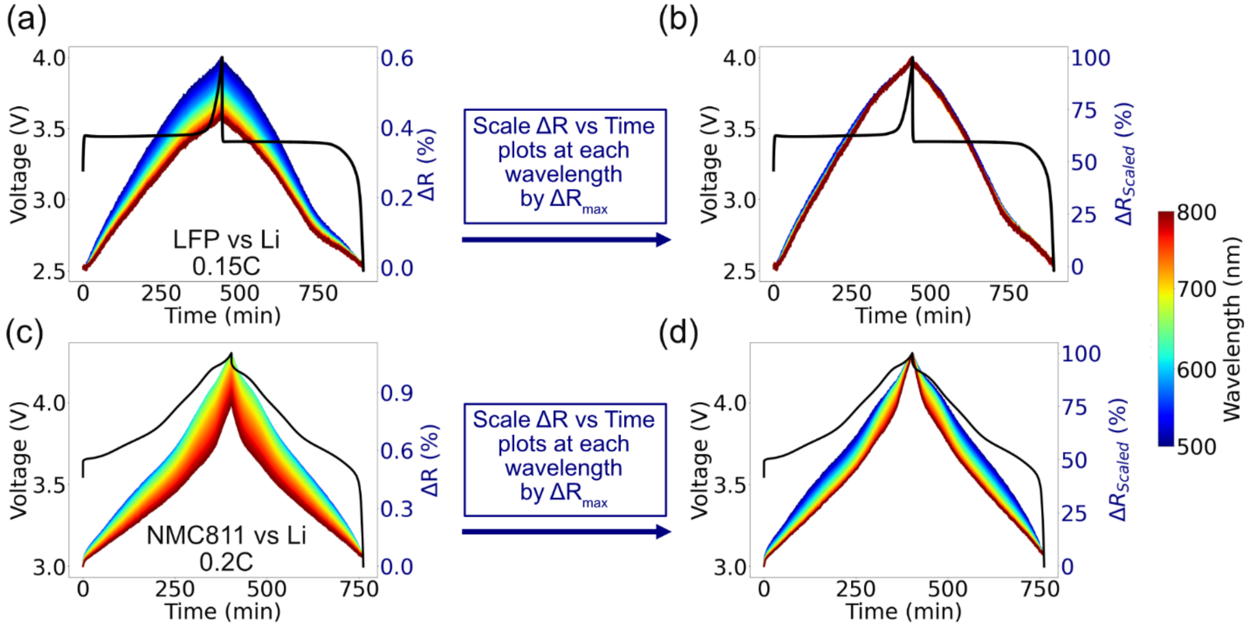

Fig. S7 Change in reflection at each wavelength (between 500 nm and 800 nm) for (a) LFP vs. Li and (c) NMC811 vs. Li. For both materials, the blue wavelengths show a greater increase in magnitude than the red wavelengths. However, each reflectance vs. time plot can be 'scaled', i.e. divided by the maximum change in its magnitude to produce scaled reflection vs. time plots, which have values between 0 and 100. This is shown for (b) LFP and (d) NMC811. For LFP, the magnitude of reflectance at all wavelengths changes at the same rate, and thus the scaled reflection vs. time plots are identical for all wavelengths. In the case of NMC811, a disparity is seen.

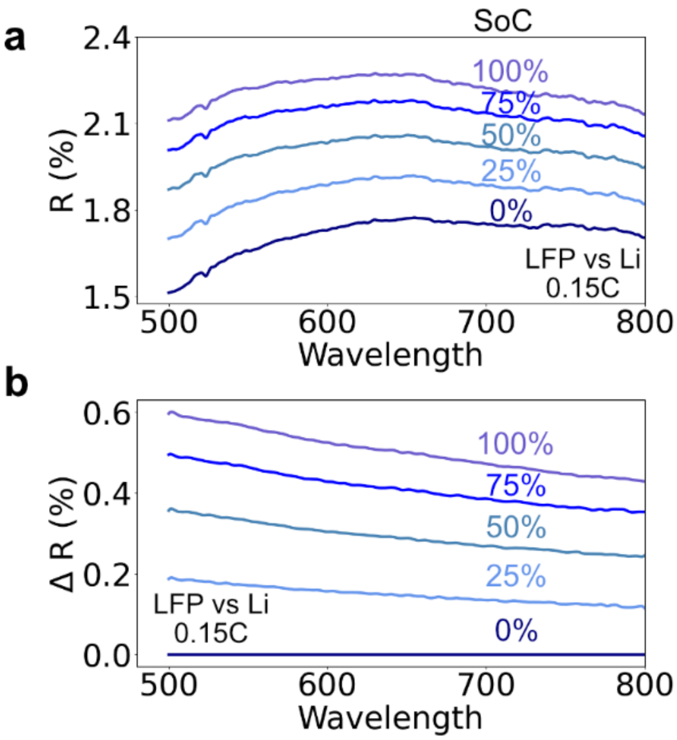

Fig. S8 (a) The visible light (500-800 nm) reflection spectrum of LFP vs Li at different SoCs. The diffuse reflectance of LFP is rather featureless in the wavelength regime shown as the main $Fe^{2+}/^{3+}$ redox peak lies in the ultraviolet regime.[15] Nevertheless, an approximately linear change in reflectance with SoC is seen. (b) Subtracted spectra, relative to the spectrum at 0% SoC. This removes any features which do not change with SoC - for example the inflection point at approximately 525 nm which originates from the optics of the system. This allows for the easy identification of any peaks which may appear.

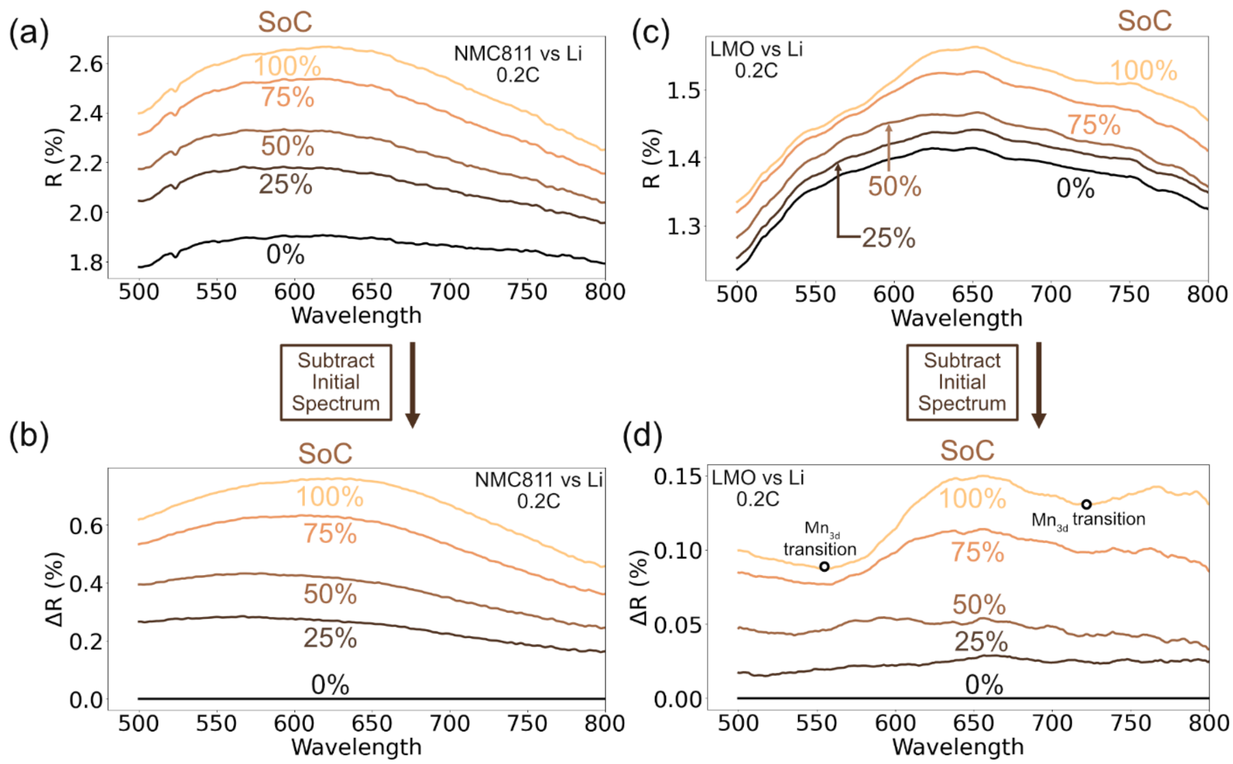

Fig. S9 Reflection spectra of (a) NMC811 and (b) LMO vs. Li as a function of SoC. Peaks in the reflection spectrum of both materials emerge at higher SoCs. This is clearer in the subtracted spectra, with a peak at 620 nm appearing for (c) NMC811 and at 650/750 nm for (d) LMO. Reflection data can be interpreted as the complement of absorption data - a peak in reflectance is associated with an absorption onset due to the associated modulation of the refractive index of the material. The reflection troughs (or absorption peaks) seen at 560 nm and 725 nm for LMO have been previously reported as corresponding to electronic transition between Mn_{3d} states.

Supplementary Note 5: Nickel Oxidation-Induced Reflectance Peaks in NMC811 Cathodes and Consequences for Optical Microscopy

In the case of NMC811, which undergoes a solid solution reaction, a visible peak in the reflection spectra at about 620 nm emerges during the charging process, as seen in **Fig.** S9(a) and (b). The charging process in NMC811 results in a change in oxidation state in nickel ($Ni^{3+/4+}$), which manifests as a peak in the reflection spectrum of the material. To further confirm this, we performed DRS on $LiNiO_2$ (the parent material of NMC811), as seen in

Fig. S10. A peak at around 660 nm emerges during the charging process. This is also due to nickel oxidation in $LiNiO_2$, however the addition of Co and Mn in NMC811 can change the Fermi level of the material, modulating its optical properties,[16] shifting the position of reflectance peaks. NMC811 develops a visible reflection peak at ∼620 nm during charging due to the oxidation of Ni^{3+} to Ni^{4+}.

The emergence of peaks in the reflection spectrum of NMC811 leads to a variation in the response of different wavelengths in the reflection vs time plots in **Fig. S7**(c) and (d). Thus, even after scaling the reflectance vs time plot, differences in behaviour exist. In LMO, which undergoes both a solid solution and phase change reaction, the appearance of new peaks in the reflectance spectrum can be seen (**Fig. S9**(d)). Reflectance can be viewed as the complement of absorbance, therefore troughs in the reflectance spectrum indicate the emergence of absorbance peaks. By comparing these spectra to absorption spectra of LMO thin films, we can assign the peaks at 550 nm and 720 nm to electronic transitions between the O-2p band and the split Mn-d band.[17,18] The phase transition at approximately 50% SoC leads to a large jump in reflectance due to the formation of an MnO_2 shell on the material.[19]

This wavelength dependent behaviour in materials with transition metals leads to complications when selecting imaging wavelengths for optical microscopy of battery particles as different illumination wavelengths will result in differing visualization of intensity changes within the electrode. For materials with a solid solution behaviour, the change in band structure (and reflectance) during ion intercalation/deintercalation should be approximately linear.[20] Thus, DRS can help inform the choice of wavelength for microscopy or to establish the reflection versus SoC calibration curve.

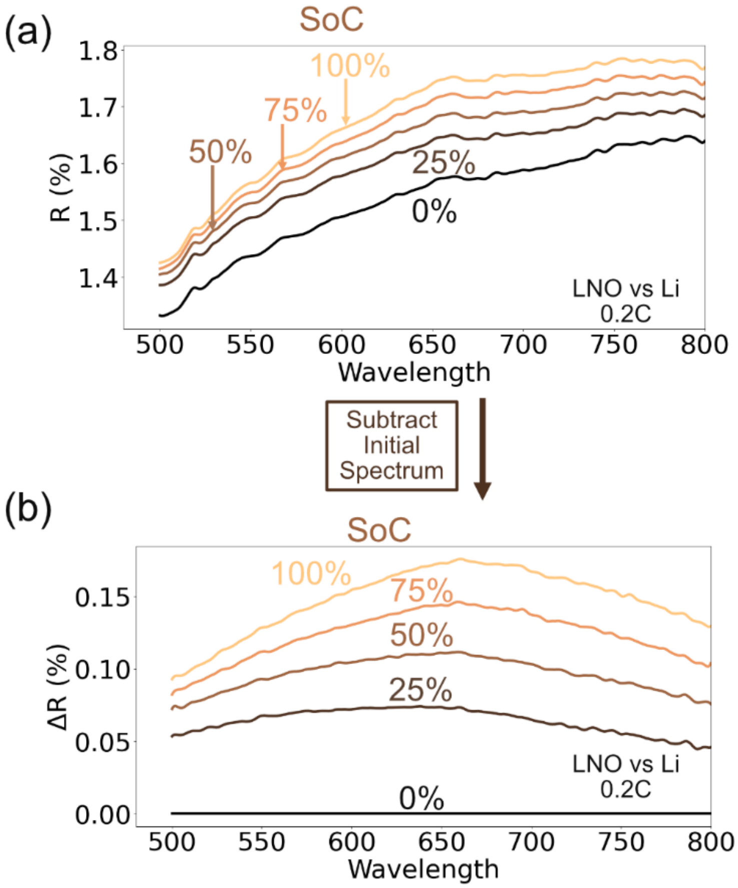

Fig. S10 Reflection spectra of $LiNiO_2$ (LNO) vs. Li as a function of SoC. (a) The entire spectrum at different SoCs. (b) Subtracted spectra, relative to the spectrum at 0% SoC. A peak at around 660 nm emerges with increasing SoC.

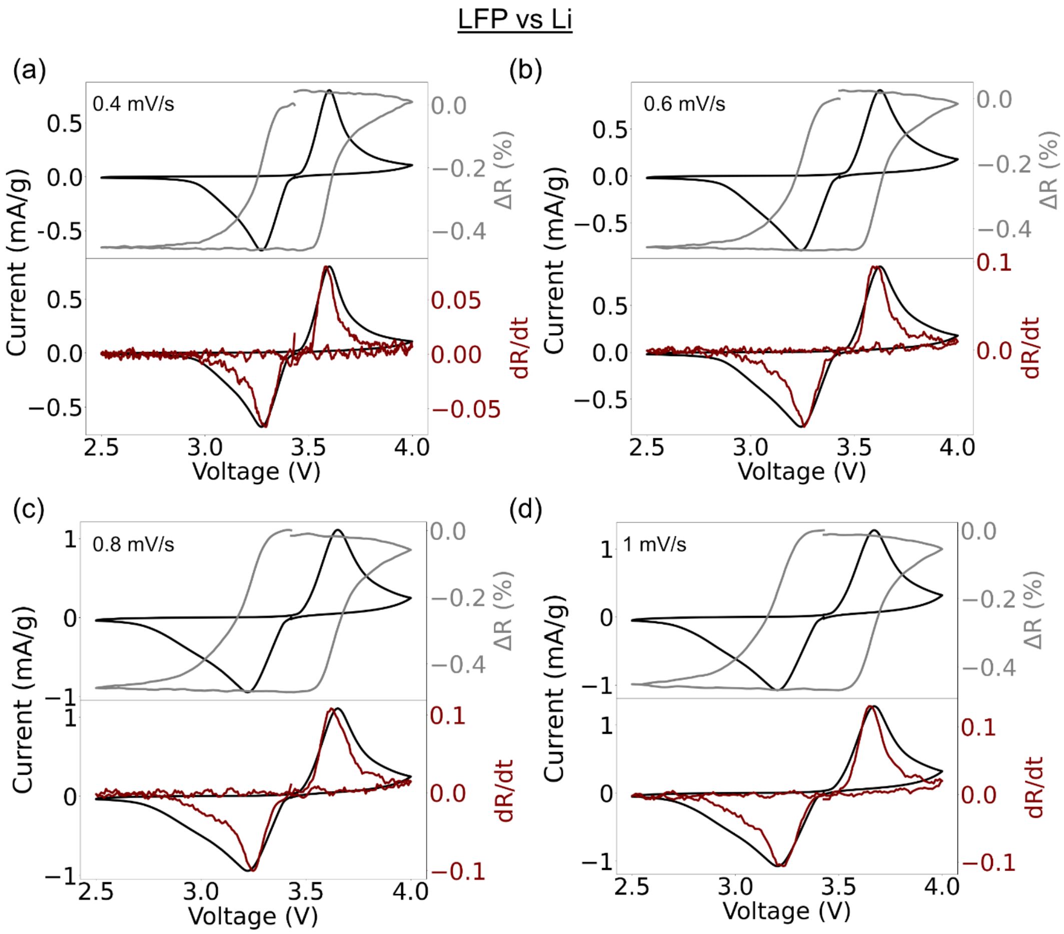

Fig. S11 CV curves for lithiated LFP at (a) 0.4 mV/s, (b) 0.6 mV/s, (c) 0.8 mV/s, (d) 1 mV/s. The top panels are the electrochemical voltage vs current (black) and reflection change vs voltage (grey) while the bottom panel contains the derivative of reflectance with time vs voltage (red), i.e. the optical CV curves. A good correlation is seen at low rates (0.4 mV/s). At higher rates, the electrochemical and optical reduction peak begin to diverge.

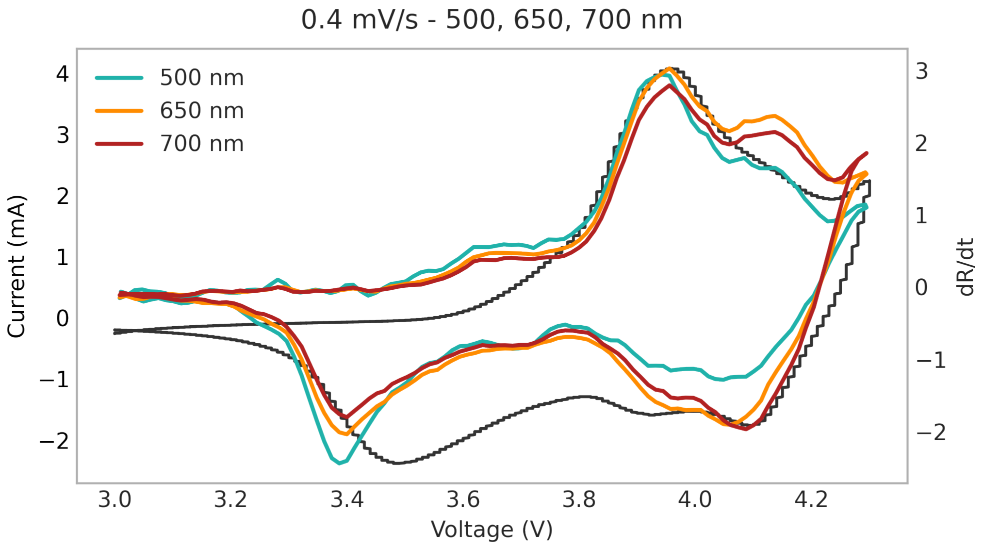

Fig. S12 CV curves of single crystal NMC811 vs Li at 0.4 mV/s at different wavelengths. A good correlation is seen between the optical and electrochemical CV curves during oxidation, with an offset seen during reduction. We note that the peak positions of the optical CV curves are the same across a range of wavelengths.

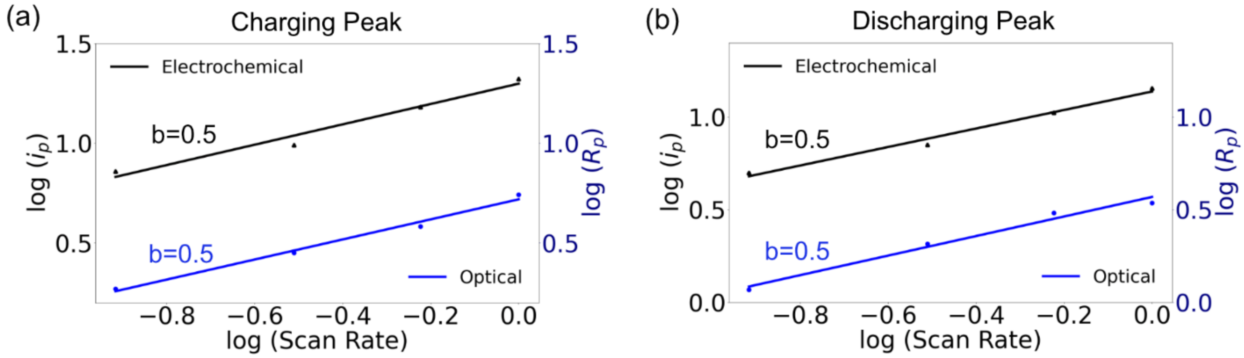

Fig. S13 Calculating b-values for the major charging and discharging peaks in cyclic voltammograms of LFP vs. Li. The current in the CV curves can be related to the scan rate using the Randles-Ševčik equation to calculate b-values. A b-value of 0.5 indicates that the current is diffusion controlled while a b-value of 1 indicates that current is capacitively controlled. As the particle size of LFP used here is several microns, there are unlikely to be any capacitive effects, which is indicated by the b-value of 0.5 in both the (a) charging and (b) discharging peaks. Interestingly, the 'optical' current, obtained by differentiating the change in reflectance with respect to time also has a b-value of 0.5, indicating the utility of this technique.

Supplementary Note 6: Sources of Error in DRS Measurements

Several potential sources of systematic error in the DRS measurements were considered. Light source intensity drift was found to be negligible over the timescales of the experiments, as demonstrated by the stability of the measured reflectance over the span of a day (**Fig.** S14). Optical contributions from the cell window were minimised using a gloss trap to suppress specular reflection, while the sealant was masked with an annular ring to prevent interference with the measurement area. In the non-transmissive configuration, the mesh current collector is obscured by the electrode and does not contribute to the DRS signal; in the transmissive configuration, the FTO current collector acts as a static thin-film layer with high specular reflectance and its reflectance is absorbed by the gloss trap. Time-dependent wetting effects were mitigated by resting all cells for 8 hours prior to cycling to ensure full electrolyte penetration. Finally, changes in scattering geometry arising from electrode swelling were assessed. For the active materials studied here, particle volume changes upon lithiation are modest - approximately 6% contraction for both LFP and NMC - and are not expected to significantly perturb the scattering geometry. This is because for large particles the scattering and absorption cross-sections are relatively agnostic to small changes in particle size. This contrasts with high-volume-change materials such as silicon, where particle expansion would substantially alter the optical response and would need to be explicitly accounted for in the DRS interpretation. Particles may also move during cycling, but one of the powerful aspects of DRS is that it averages the output of thousands of particles and therefore microscopic changes to specific particles do not change the average output.

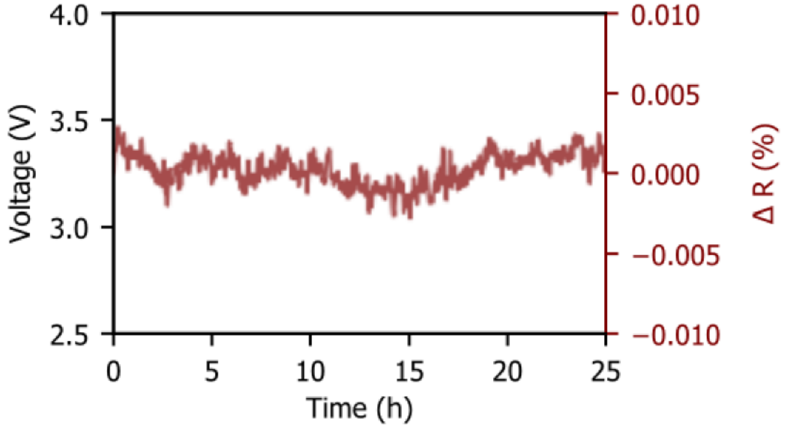

Fig. S14 Reflectance vs time for a freshly made NMC811-Li cell at 500 nm. Minimal change in reflectance is seen indicating that light source drift and thermal instabilities from the light source and cell wetting do not substantially affect the DRS spectrum over time periods of the order of a day.

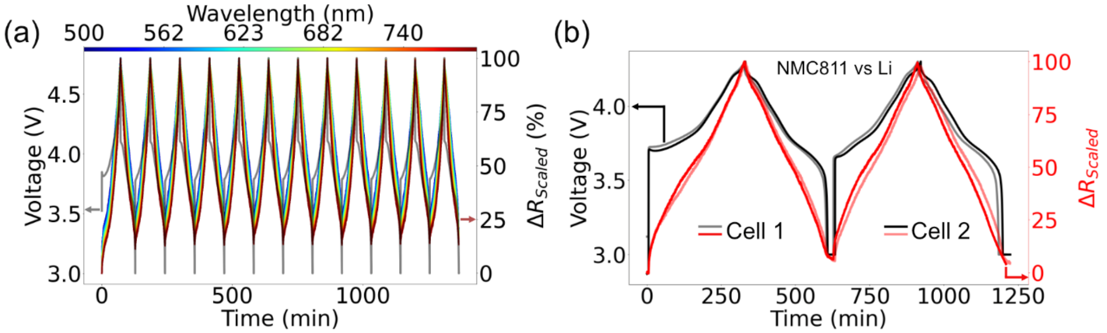

Fig. S15 Voltage vs. time and reflection vs. time curves of two different NMC811 cells cycled at 0.2C with a voltage hold at 3 V after the second discharge. Both cells display similar electrochemistry, as evidenced by their voltage vs. time plots, highlighting the reproducibility of optical cells. Small changes can be attributed to variations in ambient temperature of the room. The reflection vs. time plot at 500 nm of both cells is also remarkably similar, highlighting the reproducibility of DRS. Intriguingly, in regions where the voltages of the two cells are identical (such as the first discharge), the reflection vs. time plots are identical. Meanwhile, in regions where there is a potential difference between the cells (such as the second discharge), the plots vary at slightly different rates.

Supplementary Note 7: Diffuse vs Specular Reflectance

To highlight the necessity for diffuse reflection measurements, we track the total reflection (specular + diffuse) in **Fig.** S16(b) by removing the gloss trap in the integrating sphere. However, the reflectance changes observed are much lower when compared to just the diffuse reflectance **Fig.** S16(a). This is because the signal is dominated by the specular component from the glass window (which does not change with SoC). Thus, tracking the reflectance of the electrode through an optical fibre will only collect specular reflectance (or a part of the diffuse reflectance) and is unlikely to provide a representative measure of the SoC of the battery. Indeed, the negative changes in total reflectance seen are consistent with previous reports using an optical fibre[4] and optical microscope[21] which can only measure the specular components of reflection. This highlights the necessity of an integrating sphere for diffuse reflectance measurements of composite cathodes with a high signal-to-noise ratio.

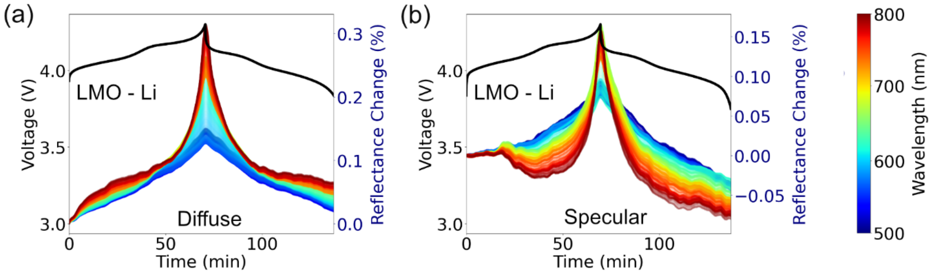

Fig. S16 Reflectance vs. time curves for LMO vs. Li using (a) diffuse reflectance and (b) specular + diffuse reflectance, i.e. the total reflectance. The reflectance changes obtained in the first case are much larger, while the changes are smaller and non-monotonic. This is because specular contributions from the glass window can also contribute to the signal. The non-monotonic rise indicates that the total reflectance cannot be correlated with SoC.

Supplementary Note 8: The Effect of Particle Crystallographic Orientation on Reflectance Measurements

To understand how crystallographic orientations of individual particles affect the reflected signal, we present microscopy data from single crystal NMC811 electrodes cycled against a Li metal anode in **Fig. S17**. In the pristine state, several bright spots are seen in the electrode. These correspond to crystallographic orientations in the material which reflect light more strongly. Upon charging, the number of bright spots increases, but does not cover the whole electrode. Thus, upon charging, other crystallographic orientations begin to reflect light more strongly, however the presence of 'darker' regions indicates that not all crystallographic orientations behave in this manner. This has two implications. Firstly, in conventional microscopic techniques which capture only a small area of the electrode, there is a possibility that brightness changes in only some crystallographic orientations are recorded, making the correlation between brightness and SoC more tenuous. Secondly, if specular reflection is collected, there is a possibility that the reflection spectrum is biased towards certain crystal planes which reflect light in a certain orientation, leading to non-monotonic increases in reflection with time. Thus, by collecting diffuse reflectance over a large area (0.64 mm^2 or about 13000 particles) we average out these inhomogeneities, resulting in a more representative picture of the SoC of the electrode.

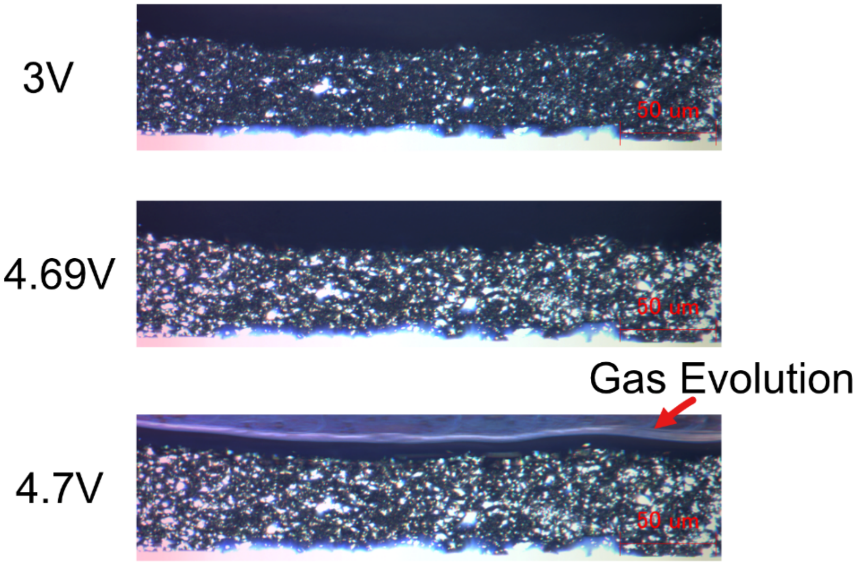

Fig. S17 Cross-sectional confocal microscopy images of single crystal NMC811 electrodes during the charging process. A few bright spots are visible, indicating that certain crystallographic orientations are brighter. After charging, the number of bright spots increases dramatically. Thus, upon lithiation, other crystallographic directions also increase in brightness dramatically. Thus, the brightness of the region heavily depends on the crystallographic orientation of the particles in that area.

Supplementary Note 9: DRS Measurements on a Commercially Available Scanning UV-vis Spectrometer Equipped with an Integrating Sphere

We demonstrate DRS using a traditional UV-vis spectrometer equipped with a 100 mm integrating sphere in **Fig.** S18. The scanning UV-vis spectrometer is a scientific instrument available in most universities for which the integrating sphere is available as a commercial add-on. To maximize the signal which can be obtained, we develop aqueous planar cells[22] consisting of Zn and $LiMn_2O_4$ deposited in a layer-by-layer fashion as shown in the inset of **Fig.** S18(d) and mount them on the spectrometer (**Fig.** S18(b)-(c)). A scanning spectrometer cannot record the entire spectrum at once but can track the temporal change in the reflectance at a certain wavelength. Therefore, we charge the cells up to different voltages and record the reflection spectrum at each voltage as shown in **Fig.** S18(e). We also track the change in reflectance at 482 nm with time and plot it in **Fig.** S18(d), demonstrating that DRS can be performed using conventionally available equipment. Although we have used planar cells here, with suitable masking of the metallic casing, the reflectance of a coin cell could also be studied.

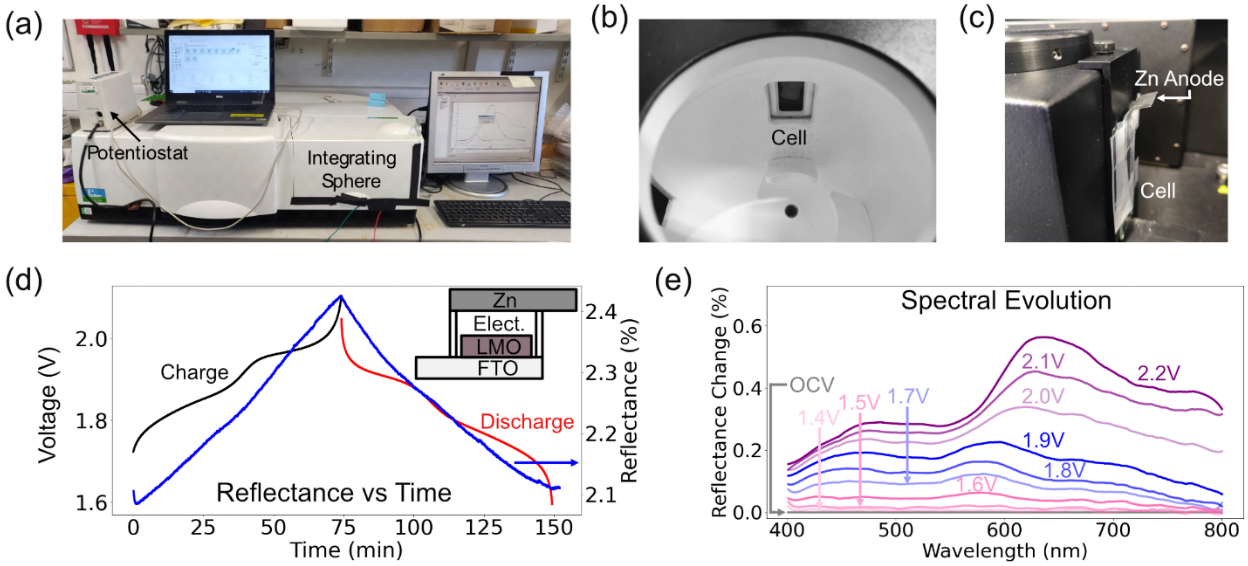

Fig. S18 Performing DRS on a commercially available UV-vis setup. A potentiostat and integrating sphere are used for this study. (b) An illustration of how the cell is mounted onto the integrating sphere for DRS measurements. (c) Another view of cell mounting. (d) Reflectance vs. time for a $LiMn_2O_4$ cathode cycled against a Zn anode using a water-in-salt-based electrolyte. The cell structure is shown in the inset. A scanning spectrometer cannot acquire the entire reflection spectrum at once; instead the reflectance at a specific wavelength can be tracked with time. (e) The evolution of reflection spectra with state of charge, with characteristic peaks corresponding to Mn_{3d} transitions emerging. This experiment highlights how any laboratory UV-vis equipped with an integrating sphere can be adapted for these measurements.

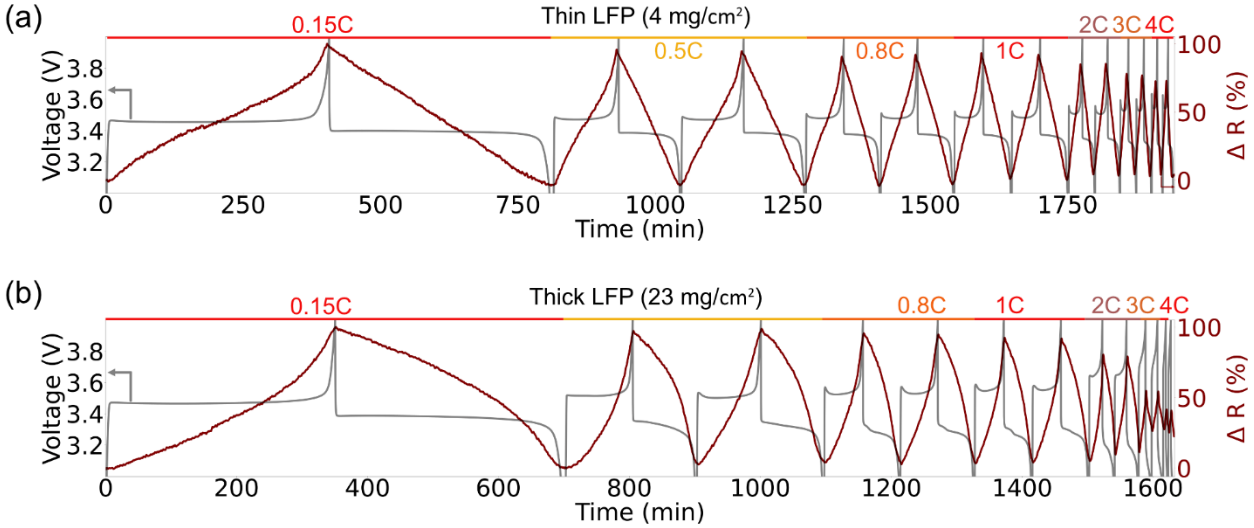

Fig. S19 Recreation of charge-discharge curves through DRS. Normalized reflection at 500 nm (red) vs. time and voltage vs. time plots (grey) curves are superimposed on the same graph. Charge/discharge was carried out sequentially at different rates (0.15C, 0.5C, 0.8C, 1C, 2C, 3C, and 4C) for (a) thin and (b) thick electrodes. A decrease in peak reflectance can be seen at higher rates.

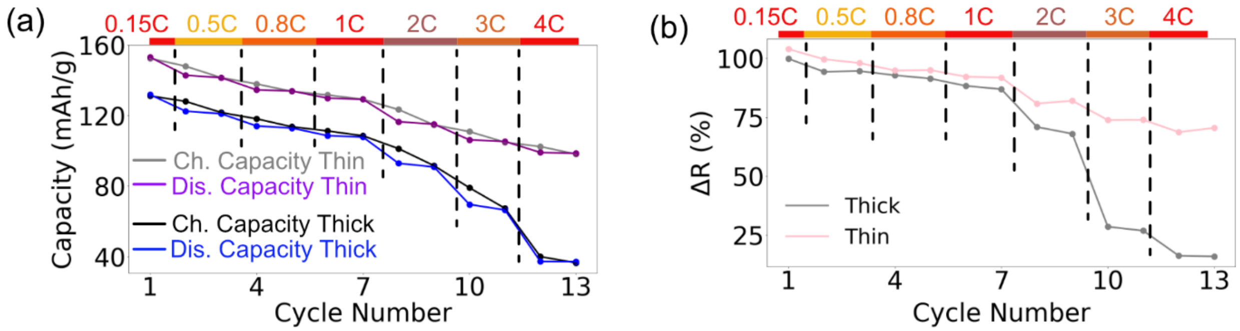

Fig. S20 (a) Capacity as a function of C-rate for the thick and thin electrodes, with a linear decrease seen for the thin electrode but exponential decrease seen for the thick electrode. (b) Change in reflectance at the top of charge as a function of C-rate, with the trends mirroring those seen in (a).

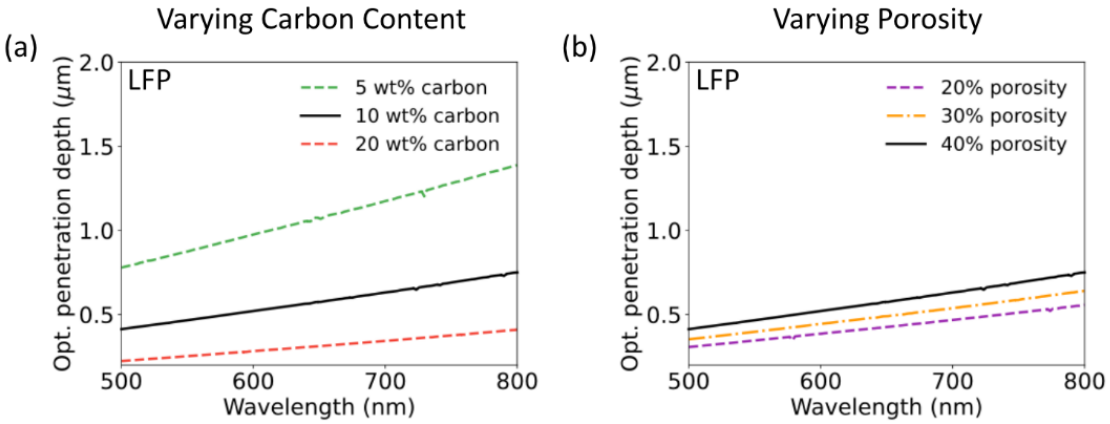

Fig. S21 The optical penetration depth of a dense LFP/carbon black/PVDF composite electrode simulated as a function of wavelength (500-800 nm) for (a) electrodes with varying carbon content and (b) electrodes with varying porosity. As the carbon content increased the optical penetration depth decreased due to strong absorption. As the porosity increased the optical penetration depth increased. In both cases the optical penetration depth was limited to less than one micron, confirming that the DRS signal acquired is from the bottom of the composite electrode. Volume fractions were derived from weight fractions using material densities ($\rho_{\text{LFP}} = 3.60$, $\rho_{\text{C}} = 1.80$, $\rho_{\text{PVDF}} = 1.78$ g cm^{-3}), assuming 40% porosity. The optical constants of LFP were taken as $n = 2.8$, $k = 0.02$.[23] The effective complex refractive index of the matrix (carbon black, PVDF, and electrolyte) was computed using the Maxwell-Garnett[24] mixing rule, with electrolyte ($n = 1.50$) as the continuous host phase and carbon black and PVDF as simultaneous spherical inclusions. Carbon black was modelled with dispersive optical constants ($n = 1.90$-2.07, $k = 0.54$-0.65 across 500-800 nm). Mie scattering efficiencies (Q_{sca}, Q_{abs}, g) for LFP particles embedded in this effective matrix were computed using the Lorenz-Mie solution and averaged over a log-normal particle size distribution (mean diameter 5 µm, $\sigma = 0.3$). Bulk scattering and absorption coefficients were derived from the particle number density and Mie efficiencies, and the optical penetration depth was calculated using the diffusion approximation, $\delta = [3\mu_a(\mu_a + \mu_s')]^{-1/2}$. It should be noted that the diffusion approximation is valid when $\mu_s' \gg \mu_a$, i.e. when the particles are large.

Supplementary Note 10: Reflection Heterogeneity Across the Depth of the Electrode

After operando cross-sectional microscopy the electrode is divided into three regions for analysis: near the separator, middle of the electrode, and near the current collector. The brightness changes in each of these regions are normalised and then compared. At low rates

(0.15C, **Fig.** S22(a)), the brightness of all three regions increases at the same rate. Since there is no 'optical' heterogeneity across the electrode, it can also be inferred that there is no electrochemical heterogeneity either. At higher rates (1C, **Fig.** S22(b)), the brightness of the region near the separator increases at a faster rate than the region in the middle and near the current collector. This indicates a degree of 'optical' and electrochemical heterogeneity within the electrode, due to reduced lithium-ion diffusion at higher rates.

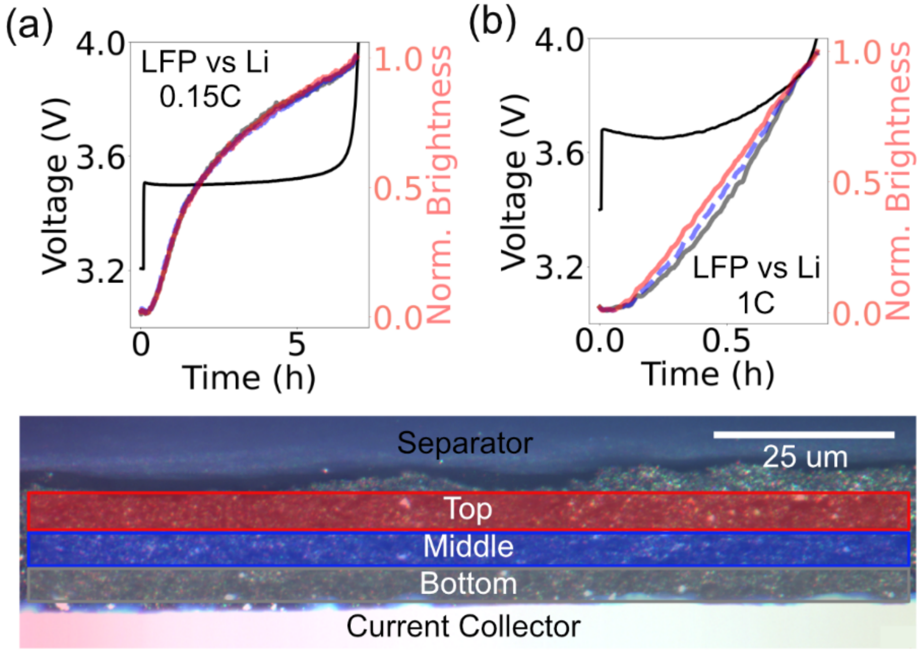

Fig. S22 Brightness changes in LFP cathodes during side view confocal microscopy at (a) 0.15C and (b) 1C charging. At low rates, the SoC of all regions of the electrodes changes at the same rate. At high rates, due to mass transport limitations, the SoC of the region near the current collectors lags behind the SoC of the region near the separator. This manifests as a lag in reflectance between these two regions of the electrode.

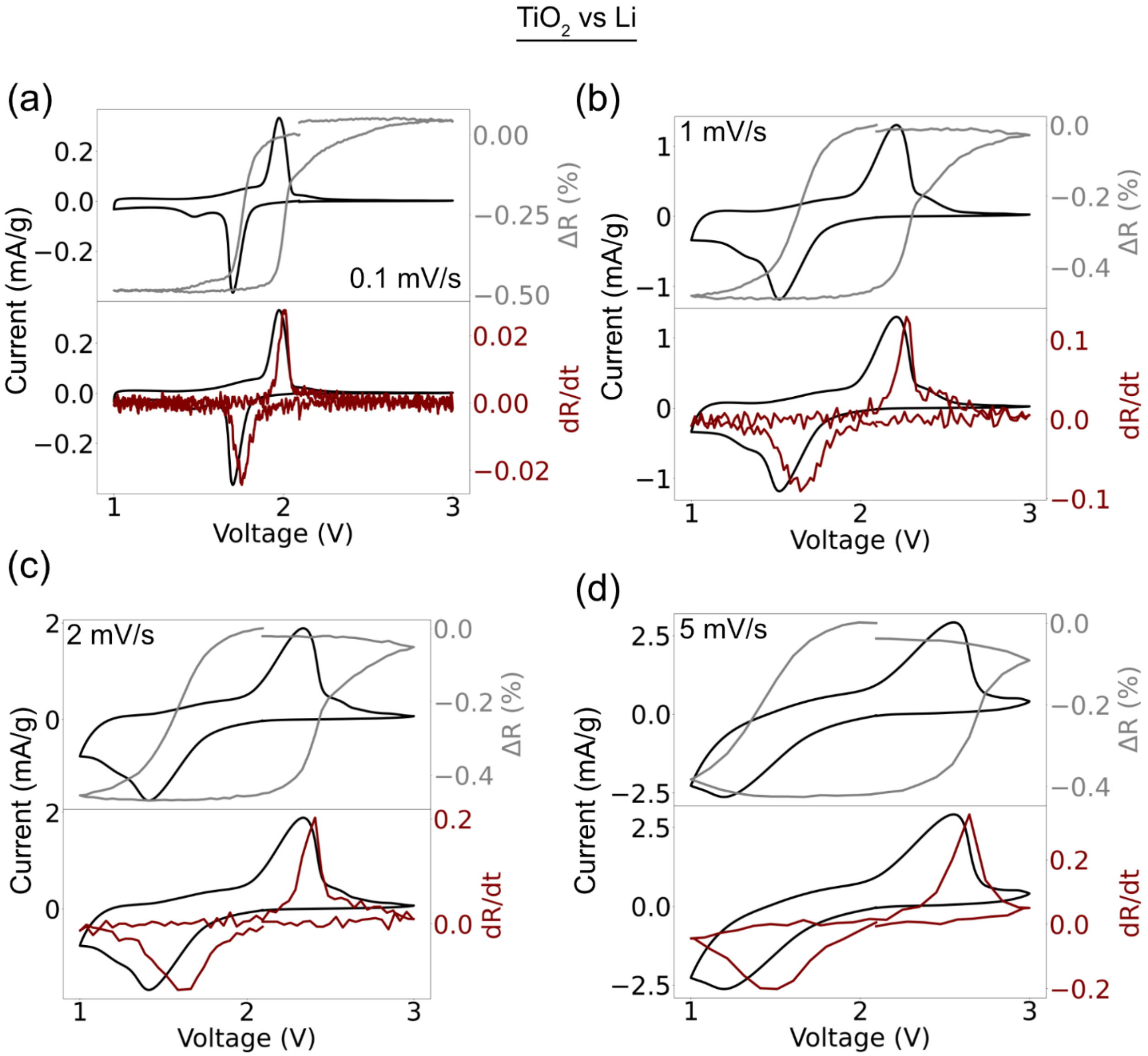

Fig. S23 CV curves for anatase TiO_2 at (a) 0.1 mV/s, (b) 1 mV/s, (c) 2 mV/s, (d) 5 mV/s. The top panels are the electrochemical voltage vs current (black) and reflectance change vs voltage (grey) while the bottom panel contains the derivative of reflectance with time vs voltage (red), i.e. the optical CV curves.

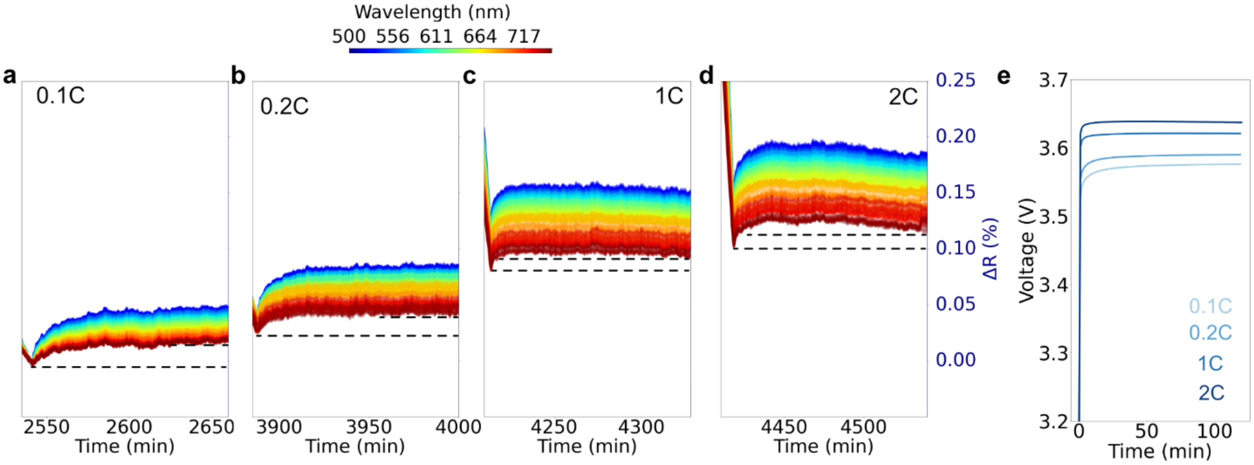

Fig. S24 Repeats of charge/discharge cycles at different rates followed by 2-hour rests at (a) 0.1C, (b) 0.2C, (c) 1C, (d) 2C. At the lower rates, the reflectance increases monotonically at all wavelengths, whereas at higher rates, a dip in reflectance is seen after the original rise, strongly mirroring the earlier results. (e) Voltage vs time plots during the rest periods after each of the discharges. The 'dip' is greater after faster discharges.

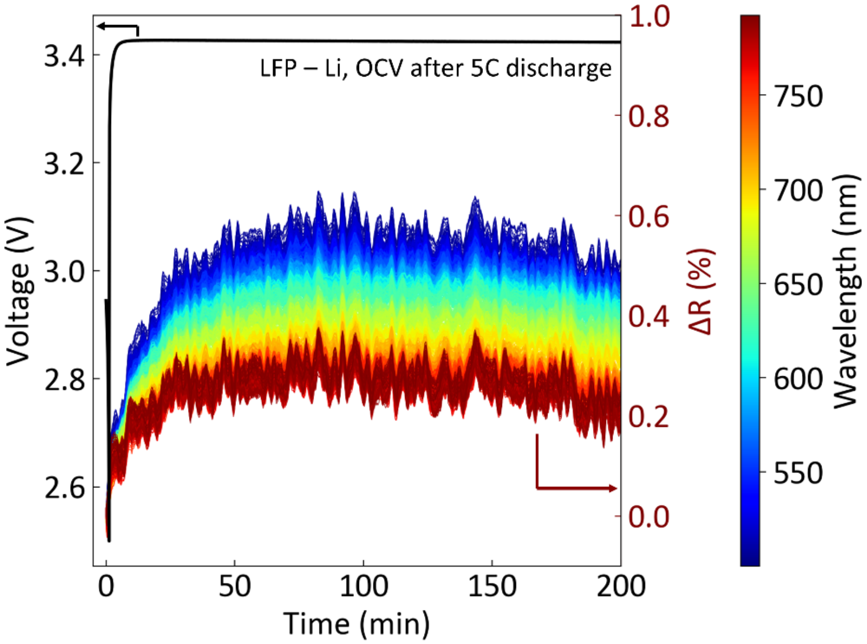

Fig. S25 Reflectance profile of an LFP-Li cell while resting after a 5C discharge. An increase and then decrease in reflectance is seen.

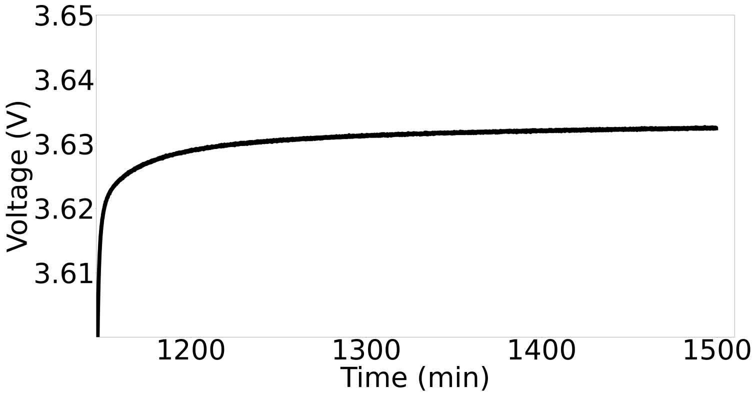

Fig. S26 Voltage profile during the relaxation post the 1C discharge.

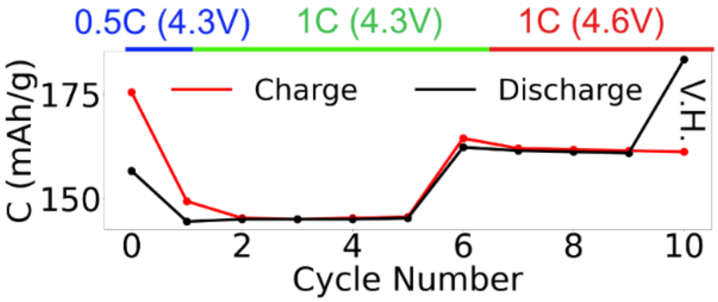

Fig. S27 Capacity vs cycle plot for NMC811 with varying upper cutoff voltages. A large first cycle capacity loss of 20 mAh/g is seen. Changing the rate to 0.5C (Cycle 2) and upper cutoff voltage to 4.8 V (Cycle 6) also results in capacity losses. A voltage hold at 3 V after cycling helps regain most of the 'lost' capacity.

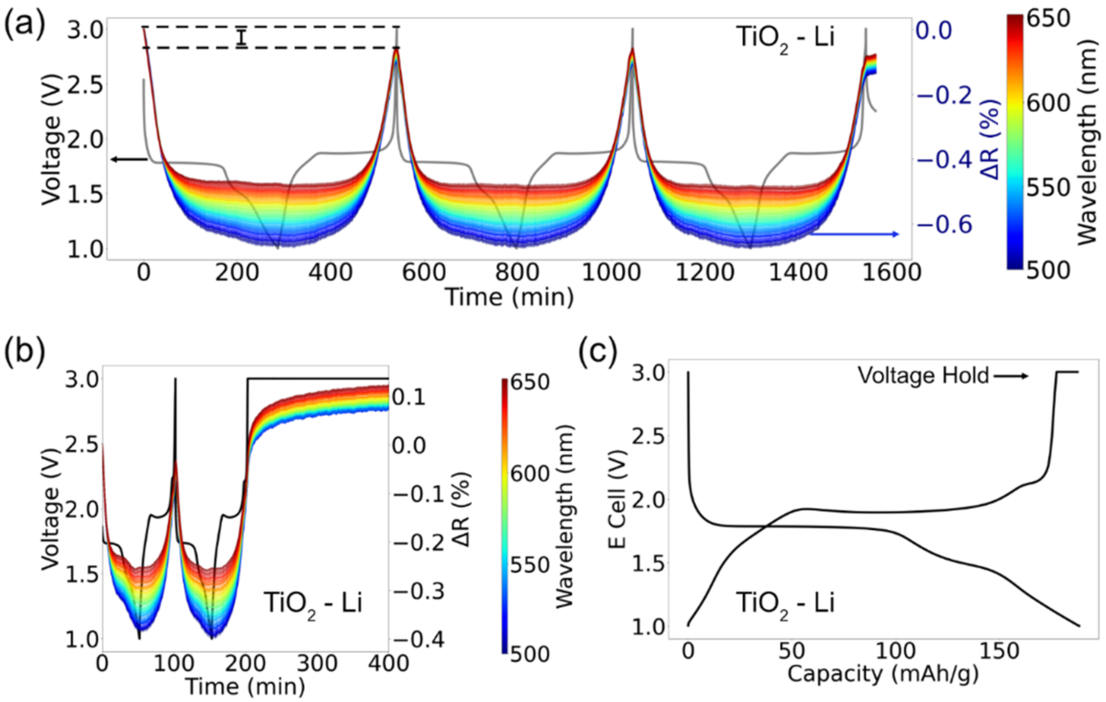

Fig. S28 Reflection vs. time curves of TiO_2 vs. Li. (a) Voltage vs. time and reflection vs. time for three cycles at 1C. During the initial 10 minutes of discharge, the reflection at all voltages decreases sharply. For the next 40 minutes, a more divergent trend is seen, with the blue wavelengths decreasing at a faster rate than the red wavelengths. This is due to the emergence of polaronic bands within the visible reflection spectrum of the material. The reflection spectrum of the material does not return to its original value, indicating that not all the lithium-ions are deintercalated from the material. (b) Subsequently, the cell is charged and discharged twice at 1C followed by a voltage hold at 3 V at the top of charge. This is to check if kinetic limitations were inhibiting the complete deintercalation of the material. An increase in reflectance is seen during the voltage hold, indicating that the SoC of the material was changing. (c) Charge-discharge curves of TiO_2 at 0.2C after incorporating a 3 V voltage hold. Although the voltage of TiO_2 increases sharply between 2.2 V and 3.0 V while charging, approximately 10 mAh/g of extra capacity can be obtained.

Supplementary Note 11: First Cycle Capacity Losses in TiO_2

We apply the same technique to the anatase TiO_2 anodes studied earlier, which have been reported to suffer from kinetic limitations.[25] When the anatase-TiO_2 anode is cycled at 0.2C, a large first cycle capacity loss was seen (**Fig.** S28), and the magnitude of reflection does not return to its original value, suggesting SoC slippage after the first charge. The voltage vs.

time discharge curve of TiO_2 increases rapidly between 2.5 to 3 V, indicating that there is not a huge amount of extra capacity in this region. However, when a voltage hold is performed at 3 V (**Fig. S28**(b)), the magnitude of reflection increases (indicative of further delithiation occurring) until the values saturates. This manifests as 10 mAh/g of extra capacity (**Fig. S28**(c)), which is lower than the 30 mAh/g lost in the first cycle, indicating that some of the lost capacity is due to kinetic limitations. More explicitly, it appears that the insulating TiO_2 shell formed around the particle during delithiation prevents complete reduction of the Ti^{3+} species deeper within the core of the particle. Understanding the timescales of lithiation/delithiation during voltage holds is crucial for managing capacity losses during kinetic limitations - for example a 24 h voltage hold was required for NMC based cathodes.[26] Thus, DRS can provide clues about the origin of lost capacity that electrochemistry on its own cannot.

References

[1] Merryweather, A. J.; Jacquet, Q.; Emge, S. P.; Schnedermann, C.; Rao, A.; Grey, C. P. Operando Monitoring of Single-Particle Kinetic State-of-Charge Heterogeneities and Cracking in High-Rate Li-Ion Anodes. *Nat. Mater.* **2022**, *21* (11), 1306-1313.

[2] Xu, C.; Merryweather, A. J.; Pandurangi, S. S.; Lun, Z.; Hall, D. S.; Deshpande, V. S.; Fleck, N. A.; Schnedermann, C.; Rao, A.; Grey, C. P. Operando Visualization of Kinetically Induced Lithium Heterogeneities in Single-Particle Layered Ni-Rich Cathodes. *Joule* **2022**, *6* (11), 2535-2546.

[3] Pandya, R.; Valzania, L.; Dorchies, F.; Xia, F.; Mc Hugh, J.; Mathieson, A.; Tan, H. J.; Parton, T. G.; Godeffroy, L.; Mazloomian, K.; Miller, T. S.; Kanoufi, F.; De Volder, M.; Tarascon, J.-M.; Gigan, S.; de Aguiar, H. B.; Grimaud, A. Three-Dimensional Operando

Optical Imaging of Particle and Electrolyte Heterogeneities inside Li-Ion Batteries. *Nat. Nanotechnol.* **2023**, *18* (10), 1185-1194.

[4] Joshi, Y.; Hadjixenophontos, E.; Nowak, S.; Lawitzki, R.; Ghosh, P. K.; Schmitz, G. Modulation of the Optical Properties of Lithium Manganese Oxide via Li-Ion De/Intercalation. *Adv. Opt. Mater.* **2018**, *6* (12), 1701362.

[5] Hedman, J.; Nilebo, D.; Larsson Langhammer, E.; Björefors, F. Fibre Optic Sensor for Characterisation of Lithium-Ion Batteries. *ChemSusChem* **2020**, *13* (21), 5731-5739.

[6] Hedman, J.; Björefors, F. Fiber Optic Monitoring of Composite Lithium Iron Phosphate Cathodes in Pouch Cell Batteries. *ACS Appl. Energy Mater.* **2022**, *5* (1), 870-881.

[7] Olgo, A.; Genies, S.; Franchi, R.; Septet, C.; Jacquet, Q.; Berrod, Q.; Palm, R.; Chenevier, P.; Villemin, E.; Villevieille, C.; Blanc, N.; Tardif, S.; Raccurt, O.; Lyonnard, S. Revealing How Internal Sensors in a Smart Battery Impact the Local Graphite Lithiation Mechanism. *Nat. Commun.* **2024**, *15* (1), 10258.

[8] Loeb, S.; Li, C.; Kim, J.-H. Solar Photothermal Disinfection Using Broadband-Light Absorbing Gold Nanoparticles and Carbon Black. *Environ. Sci. Technol.* **2018**, *52* (1), 205-213.

[9] Erraji, A.; Masrour, R.; Xu, L. Ab Initio Study of $LiMn_2O_4$ Cathode: Electrochemical and Optical Properties for Li-Ion Batteries and Optoelectronic Devices. *Ionics* **2024**, *30* (12), 7917-7928.

[10] First-Principle Study on Optical Properties of N-La-Codoped Anatase TiO. *Chin. Phys. B* **2013**, *22* (5), 057801.

[11] Pujari, A.; Kim, B.; Greenham, N. C.; De Volder, M. Identifying Current Collectors That Enable Light-Battery Interactions. *Small Methods* **2024**, *8* (10), 2301572.

[12] Bouteau, G.; Van-Nhien, A. N.; Sliwa, M.; Sergent, N.; Lepretre, J.-C.; Gachot, G.; Sagaidak, I.; Sauvage, F. Effect of Standard Light Illumination on Electrolyte's Stability of Lithium-Ion Batteries Based on Ethylene and Di-Methyl Carbonates. *Sci. Rep.* **2019**, *9* (1), 135.

[13] Pujari, A.; Merryweather, A. J.; Schnedermann, C. Optimal Coin Cell Design for Operando Optical Characterisation of Lithium-Ion Batteries. *J. Electrochem. Soc.* **2026**, *173* (1), 010505.

[14] Son, B.; Ryou, M.-H.; Choi, J.; Lee, T.; Yu, H. K.; Kim, J. H.; Lee, Y. M. Measurement and Analysis of Adhesion Property of Lithium-Ion Battery Electrodes with SAICAS. *ACS Appl. Mater. Interfaces* **2014**, *6* (1), 526-531.

[15] Zhang, Y.; Alarco, J. A.; Best, A. S.; Snook, G. A.; Talbot, P. C.; Nerkar, J. Y. Re-Evaluation of Experimental Measurements for the Validation of Electronic Band Structure Calculations for $LiFePO_4$ and $FePO_4$. *RSC Adv.* **2019**, *9* (2), 1134-1146.

[16] White, J. L.; Gittleson, F. S.; Homer, M.; El Gabaly, F. Nickel and Cobalt Oxidation State Evolution at Ni-Rich NMC Cathode Surfaces during Treatment. *J. Phys. Chem. C* **2020**, *124* (30), 16508-16514.

[17] Lee, A.; Vörös, M.; Dose, W. M.; Niklas, J.; Poluektov, O.; Schaller, R. D.; Iddir, H.; Maroni, V. A.; Lee, E.; Ingram, B.; Curtiss, L. A.; Johnson, C. S. Photo-Accelerated Fast Charging of Lithium-Ion Batteries. *Nat. Commun.* **2019**, *10* (1), 4946.

[18] Lee, S. T.; Raveendranath, K.; Tomy, M. R.; Paulraj, M.; Jayalekshmi, S.; Ravi, J. Evidence of Band Structure Modification of $LiMn_2O_4$ upon Lithium Deintercalation by Photoacoustic Spectroscopy. *Appl. Phys. Lett.* **2007**, *90* (16), 161912.

[19] Kanamura, K.; Naito, H.; Yao, T.; Takehara, Z. Structural Change of the $LiMn_2O_4$ Spinel Structure Induced by Extraction of Lithium. *J. Mater. Chem.* **1996**, *6* (1), 33-36.

[20] Zhang, D.; Wang, R.; Wang, X.; Gogotsi, Y. In Situ Monitoring Redox Processes in Energy Storage Using UV-Vis Spectroscopy. *Nat. Energy* **2023**, *8* (6), 567-576.

[21] Banifarsi, S.; Joshi, Y.; Lawitzki, R.; Csiszár, G.; Schmitz, G. Optical Modulation and Phase Distribution in $LiCoO_2$ upon Li-Ion De/Intercalation. *J. Electrochem. Soc.* **2022**, *169* (4), 046509.

[22] Pujari, A.; Kim, B.-M.; Sayed, F. N.; Sanders, K.; Dose, W. M.; Mathieson, A.; Grey, C. P.; Greenham, N. C.; De Volder, M. Does Heat Play a Role in the Observed Behavior of Aqueous Photobatteries? *ACS Energy Lett.* **2023**, *8* (11), 4625-4633.

[23] Kinyanjui, M. K.; Axmann, P.; Wohlfahrt-Mehrens, M.; Moreau, P.; Boucher, F.; Kaiser, U. Origin of Valence and Core Excitations in $LiFePO_4$ and $FePO_4$. *J. Phys. Condens. Matter* **2010**, *22* (27), 275501.

[24] Markel, V. A. Introduction to the Maxwell Garnett Approximation: Tutorial. *JOSA A* **2016**, *33* (7), 1244-1256.

[25] Hua, X.; Liu, Z.; Fischer, M. G.; Borkiewicz, O.; Chupas, P. J.; Chapman, K. W.; Steiner, U.; Bruce, P. G.; Grey, C. P. Lithiation Thermodynamics and Kinetics of the TiO_2(B) Nanoparticles. *J. Am. Chem. Soc.* **2017**, *139* (38), 13330-13341.

[26] Zhou, H.; Xin, F.; Pei, B.; Whittingham, M. S. What Limits the Capacity of Layered Oxide Cathodes in Lithium Batteries? *ACS Energy Lett.* **2019**, *4* (8), 1902-1906.